Research Square

Preprints are preliminary reports that have not undergone peer review.
They should not be considered conclusive, used to inform clinical practice,
or referenced by the media as validated information.

Backfolded slab in the mantle transition zone as a melt source for Mariana petit-spot volcanism

Ting Yang

tyang@sustech.edu.cn

SUSTech https://orcid.org/0000-0002-3433-0898

Junguo Lin

https://orcid.org/0009-0009-4271-8727

Shifei Jia

SUSTech

Zhenggang Li

Second Institute of Oceanography, MNR, China

Yongshun Chen

Department of Ocean Science and Engineering, Southern University of Science and Technology

Douglas Wiens

Washington University https://orcid.org/0000-0002-5169-4386

Article

Keywords:

Posted Date: November 9th, 2026

DOI: https://doi.org/10.21203/rs.3.rs-11408053/v1

License: This work is licensed under a Creative Commons Attribution 4.0 International License.
Read Full License

Additional Declarations: There is **NO** Competing Interest.

Backfolded slab in the mantle transition zone as a melt source for Mariana petit-spot volcanism

Junguo Lin[1], Ting Yang[1,2], Shifei Jia[1,3], Zhenggang Li[4], Yongshun Chen[1], and Douglas A. Wiens[5]

[1] OBS Laboratory, Department of Ocean Science and Engineering, Southern University of Science and Technology, Shenzhen, China.

[2] Shanghai Sheshan National Geophysical Observatory, Shanghai, China.

[3] Fujian Earthquake Agency, Fuzhou, China.

[4] State Key Laboratory of Submarine Geoscience, Second Institute of Oceanography, Ministry of Natural Resources, Hangzhou, China.

[5] Department of Earth, Environmental, and Planetary Sciences, Washington University in St. Louis, St Louis, MO USA.

Corresponding author: Ting Yang (tyang@sustech.edu.cn)

Abstract

Petit-spot volcanoes are a distinct class of intraplate volcanism whose melt source remains poorly constrained. Near the Mariana Trench, young edifices atop the incoming Pacific plate are interpreted as petit-spot features. Here we image the upper mantle beneath the central Mariana subduction zone using newly acquired and existing seafloor seismic data. Our model reveals pronounced backward folding of the subducting slab within the mantle transition zone (MTZ)—produced as ongoing subduction and the globally significant IBM trench advance feed slab material into the MTZ faster than its slowly migrating deep limb escapes, so the accumulating slab volume—accommodated by flattening and stacking—mechanically extrudes ambient MTZ material upward. We image this upwelling as a low-velocity channel extending from the MTZ to the incoming lithosphere behind the slab. Upon crossing the 410-km discontinuity, the upwelled hydrous and carbonated material releases a dense supercritical melt that ascends to form an interconnected, volatile-charged carbonate melt network at shallower depths. This deep-sourced, CO_2–H_2O-driven melting framework explains both the imaged low-velocity anomalies and the distinctive carbon-rich, alkaline geochemistry of petit-spot lavas. These findings demonstrate that trench-advance-driven slab folding can generate deep-sourced melts, offering a new perspective on intraplate volcanism and deep volatile cycling.

Petit-spot volcanoes represent a recently discovered class of seafloor volcanism, typically occurring near the outer rise of subducting plates[1–6]. Unlike island-arc, mid-ocean ridge, or hotspot volcanism, petit-spot systems are characterized by young, small-scale, spatially clustered edifices enriched in water and carbon, and occur in tectonic settings traditionally considered inhospitable to melt generation[7]. Although several mechanisms have been proposed for melt transport to the surface—including flexural faulting and lithospheric fracturing near the outer rise[1,7]—none has gained universal acceptance, so the fundamental question of where the melt originates and how it is generated in the mantle remains largely unanswered. Geodynamic modelling has proposed that slab–mantle transition zone (MTZ) interactions, such as rollback or folding, may uplift hydrous MTZ material into the upper mantle, triggering partial melting that could feed scattered petit-spot volcanoes[8,9]. To date, however, direct observational evidence for such slab-driven melting processes has been lacking.

The incoming Pacific plate beneath the central Mariana subduction zone hosts numerous seamounts—collectively termed the Western Pacific Seamount Province (WPSP)[10,11]—which are predominantly Cretaceous to Jurassic in age. Recent seafloor surveys, however, have revealed evidence of secondary, rejuvenated volcanic activity atop these ancient guyots[12–15] (Fig. 1). Dredged samples and high-resolution bathymetry confirm that these secondary edifices formed recently, with some as young as the Pleistocene, and display the defining characteristics of petit-spot volcanoes. Independent support comes from active-source reflection and refraction surveys of the incoming plate near the trench, which imaged reduced crustal velocities and disrupted sedimentary stratigraphy—characteristic features of petit-spot volcanism[16] —indicating geologically recent magmatic activity[17]. Given their proximity to confirmed petit-

spot volcanoes in the northern Mariana region and their occurrence in a similar tectonic setting[2], these features very likely represent genuine petit-spot volcanism. Yet the melt source for these young volcanic edifices remains unidentified—whether it originates from shallow lithospheric processes or from deeper slab–mantle interactions is unknown.

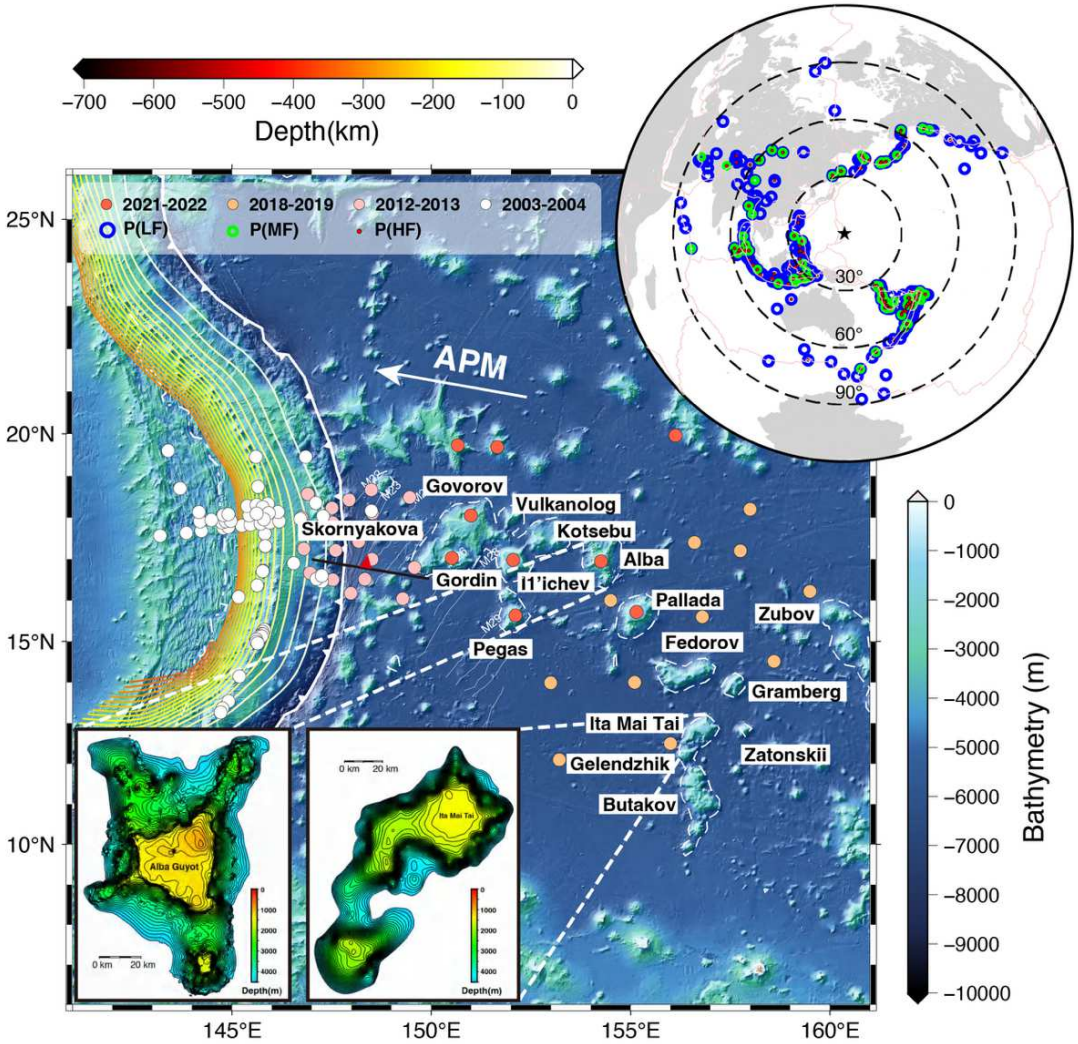


Fig. 1 | Bathymetry, seismic station distribution, and seamounts in the Mariana region. The line with triangles marks the subduction trench, yellow gradient contours denote slab depth, and white dashed lines outline the approximate extents of seamounts hosting identified petit-spot volcanoes; detailed bathymetric

maps of two such seamounts (Alba Guyot and Ita Mai Tai) are shown in the lower-left insets. The black line with a red triangle indicates the active-source survey lines[17], along which sedimentary evidence for petit-spot volcanism was identified. The upper-right inset shows the spatial distribution of earthquakes used in the high-, intermediate-, and low-frequency finite-frequency tomography.

Imaging the mantle structure beneath the incoming plate is critical to constraining the genesis of petit-spot volcanism. However, most previous seismic studies have focused on the subducting slab and back arc[18–20], leaving the upper mantle beneath the incoming plate poorly resolved. Here we combine newly deployed ocean-bottom seismographs with existing seismic arrays to image both the subducting slab and the upper mantle behind it in the central Mariana subduction zone. Our model reveals backward slab folding within the MTZ and an associated low-velocity channel extending into the upper mantle behind the slab. We interpret this folding as the mechanical fingerprint of the ongoing westward advance of the Izu-Bonin–Mariana trench—the most significant trench advance on Earth today[21–24]. We further propose that the folding mechanically extrudes volatile-rich MTZ material, whose ascent and melting supply a deep melt source for the petit-spot volcanoes on the incoming plate.

Seismic imaging of the upper mantle beneath central Mariana

We combine data from two recently deployed ocean-bottom seismic arrays in the WPSP—one during 2021–2022 (this study) and the Oldest-1 array deployed during 2018–2019[25,26]—with existing

networks[27,28] to construct a three-dimensional P-wave velocity model of the upper mantle, the MTZ, and the uppermost lower mantle (~900 km depth). The tomographic inversion employs finite-frequency, multi-band sensitivity kernels[29–31], with full details on data coverage, processing workflows, inversion parameters, and model resolution provided in the Methods and Extended Data.

The resulting model reveals two key structural features in the upper mantle beneath the central Mariana subduction zone: (1) a complex geometry of the subducting Pacific slab within the MTZ, and (2) distinct low-velocity anomalies on both sides of the slab (Fig. 2 and Extended Data Fig. 4). Across all five cross-sections (A–A' to E–E'), the slab appears as a coherent high-velocity body descending steeply from the upper mantle into the MTZ, closely tracked by intermediate- and deep-focus seismicity. Notably, as the slab approaches the upper part of the MTZ, it undergoes pronounced backward folding—most clearly expressed in profiles A–A' and B–B'—bending eastward, toward the trench, after an initial westward dip, and forming a hooked or L-shaped structure. With the inversion grid extended to 900 km, the high-velocity anomaly continues into the lower mantle directly beneath the easternmost extent of the folded slab, indicating that the buckle sits atop a slab that has penetrated the 660-km discontinuity.

We acknowledge that, because ray coverage at MTZ depths beneath the seafloor array is limited, the anomaly amplitude weakens and the folded geometry becomes progressively more blurred with depth, and below ~700 km the resolution is further damped (Extended Data Figs. 5 and 6); the dashed grey outlines in Fig. 2 are interpretive guides to the slab geometry where resolution is poor. Nevertheless, the folding and its deep continuation are robust features of the model rather than imaging artifacts: the same first-order geometry is reproduced in all five profiles and in both independent half-dataset inversions (Extended Data

Figs. 9 and 10), and targeted restoration tests—including an input model in which the slab extends into the lower mantle—recover both structures without introducing spurious eastward smearing, ruling out artifacts of limited data coverage, ray-path smearing, or the model bottom edge (Extended Data Fig. 8). Slab folding beneath the IBM system has previously been inferred only from global- and large-regional-scale models[32–35]; our study captures this deformation, and its penetration into the lower mantle, with unprecedented local detail.

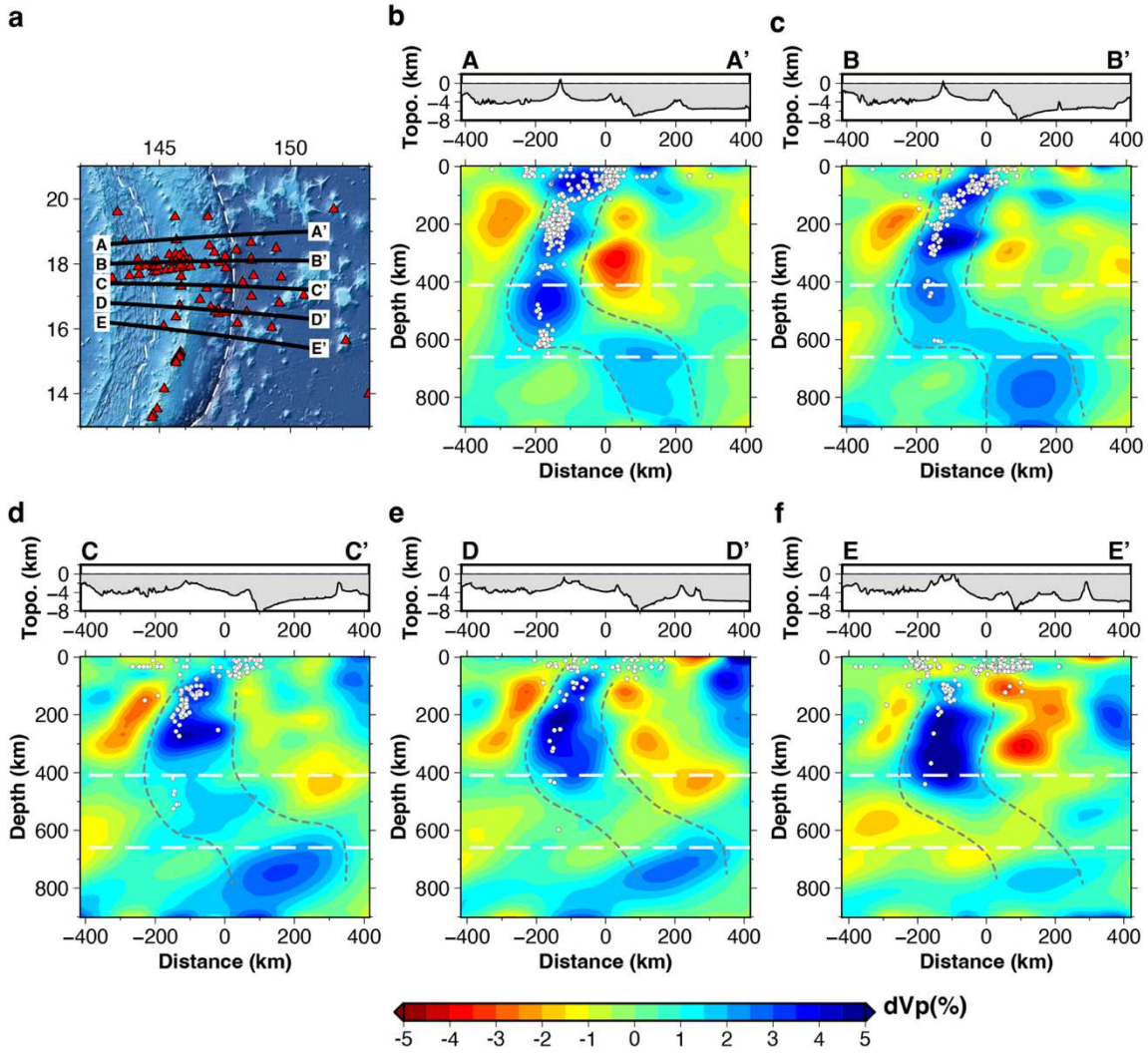


Fig. 2 | Finite-frequency tomographic inversion results beneath the central Mariana subduction zone, with the inversion grid extended to 900 km depth. a, Bathymetric map showing seismic stations (red triangles) and cross-section locations (black lines). **b–f,** Topographic profiles (top) and P-wave velocity perturbation cross-sections (bottom) along profiles A–A' to E–E'. The high-velocity slab descends into the mantle transition zone, folds backward at ~450–600 km depth, and continues into the lower mantle beneath the easternmost extent of the fold. Dashed grey lines are interpretive outlines of the slab where resolution is limited. White circles indicate earthquake hypocentres; white dashed lines mark the 410-km and 660-km discontinuities. Colors denote dVp relative to the reference model.

Accompanying this folded slab geometry are two prominent low-velocity anomalies. To the west of the slab lies the classic mantle wedge anomaly, consistent with hydrated, hot mantle above the slab. In contrast, to the east of the slab—beneath the incoming Pacific plate—we image a second low-velocity anomaly that originates near the folded segment of the slab within the MTZ and extends vertically upward into the upper mantle behind the slab, terminating near the lithosphere–asthenosphere boundary (LAB). This anomaly is clearly resolved in several profiles, where it appears as a loosely connected, scattered but vertically coherent column of reduced velocities ($\Delta Vp \approx -3\%$ to -5%). Such velocity reductions are consistent with the presence of hydrous fluids, partial melt, or thermally perturbed mantle. Critically, this eastern low-velocity channel aligns spatially with the locations of young petit-spot volcanoes on the seafloor, suggesting a direct geodynamic link between deep slab–MTZ interactions and shallow intraplate volcanism.

Backward slab folding in the mantle transition zone driven by trench advance

The L-shaped or "hooked" geometry of the subducting Pacific slab imaged within the MTZ beneath the central Mariana trench (Fig. 2) represents a mechanical buckling structure produced by recent trench advance. This deformation arises from compressional stresses transmitted through the overriding Philippine Sea Plate (PSP) during trench advance[24,36], combined with resistance encountered at the 660-km discontinuity[37] (Fig. 3).

Regional plate reconstructions and geodynamic models indicate that the Izu-Bonin-Mariana (IBM) trench underwent a dramatic kinematic shift from retreat to advance between ~8 and 5 Ma[22,23,38]. The advance is ultimately driven by slab pull from the Ryukyu subduction zone acting across the PSP[24,39]. Because the Mariana Trough is currently undergoing active back-arc spreading, which mechanically decouples the Ryukyu slab pull from the Mariana trench, the Mariana segment advances more slowly than the Izu-Bonin segment to the north, being laterally dragged by the advancing Izu-Bonin trench[21,24].

The magnitude of cumulative trench advance depends on the adopted absolute reference frame. In the dynamically preferred Indo-Atlantic hotspot reference frame[21], the Mariana trench advances at ~1.5–2.0 cm/yr, yielding a cumulative westward displacement of approximately 100–160 km over the past 5–8 Myr. In the Pacific hotspot reference frame, the advance rate could be as high as ~4.5 cm/yr, implying a displacement exceeding 300 km since 8 Ma. Regardless of the reference frame adopted, this tens-to-

144 hundreds of kilometers of forced trenchward motion at the surface stands in stark contrast to the slower
145 westward migration of the deep slab that has already penetrated the 660-km discontinuity.

146 This kinematic mismatch—rapid trenchward motion of the shallow slab versus slower motion at
147 depth—generates compressive stress more than sufficient to mechanically buckle the ~100-km-thick
148 Pacific slab, forcing the intervening slab to flatten, stack, and fold backward within the MTZ into the
149 configuration imaged in our tomographic model (Fig. 2; schematized in Fig. 3f). Geodynamic experiments
150 demonstrate that slabs encountering the 660-km discontinuity buckle when subjected to horizontal forcing,
151 without requiring unrealistically high slab viscosities[36,37,40,41], perhaps due to weakening resulting from
152 grain-size reduction as olivine transforms to wadsleyite[42].

153 It is instructive to place our observations within the broader context of the entire IBM subduction
154 system. Both the Mariana and Izu-Bonin segments have undergone significant trench advance since ~8–5
155 Ma. While earlier models depicted the Izu-Bonin slab as a gently dipping feature, recent high-resolution
156 imaging has revealed that it, too, experiences profound deformation in the MTZ, characterized by localized
157 tearing, severe buckling, and even complete overturning of the slab tip[35]. Strikingly, this widespread slab
158 contortion along the IBM system is mirrored by the surface distribution of petit-spot volcanism. In addition
159 to the well-documented petit-spots near the Mariana Trench, recent surveys have confirmed the presence
160 of young, genuine petit-spot volcanoes on the incoming Pacific plate seaward of the Izu-Bonin segment[2].
161 The co-occurrence of intense slab deformation in the MTZ and petit-spot volcanism on the incoming plate
162 in both segments strongly suggests that these are not isolated local anomalies. Instead, they represent a

systematic, regional-scale mechanical response of the IBM slab to sustained trenchward forcing against the 660-km discontinuity.

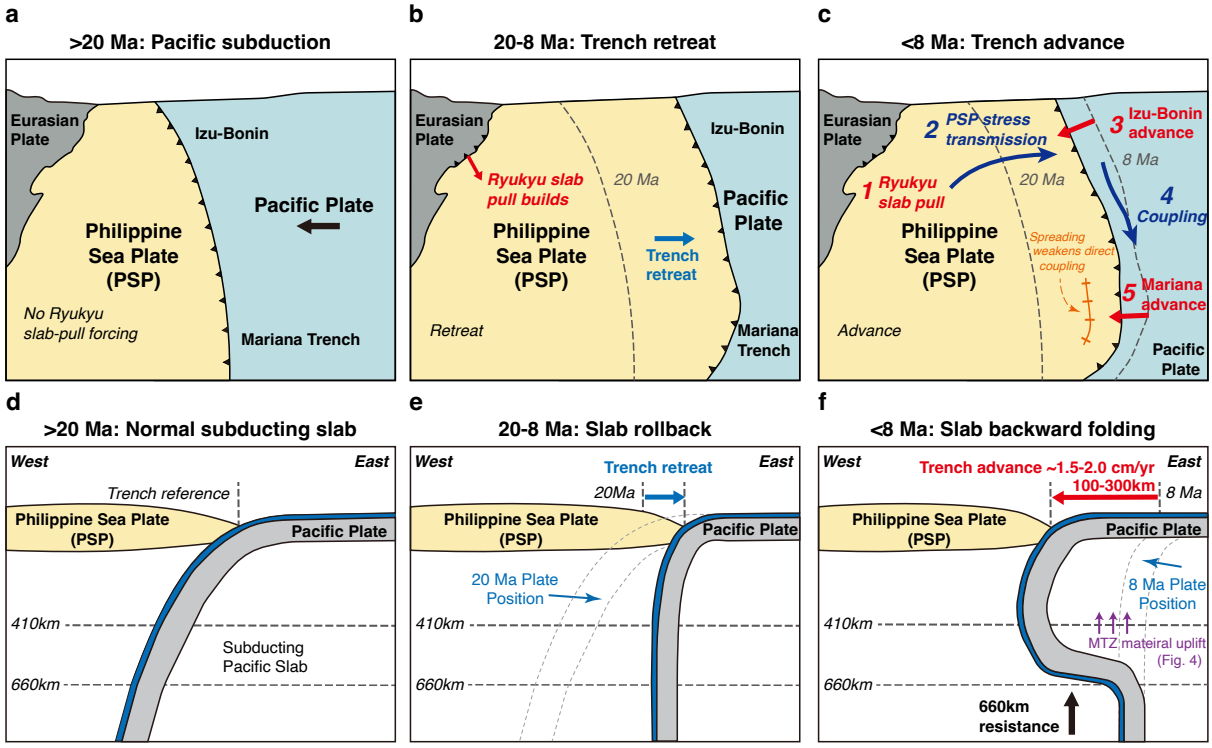


Fig. 3 | Dynamic and kinematic evolution of the Pacific slab beneath the Izu-Bonin–Mariana subduction system. a–c, Map views of the double-subduction system (barbs on the overriding plate): Pacific subduction prior to 20 Ma without Ryukyu slab-pull forcing (**a**); Ryukyu slab pull building during trench retreat and slab rollback, ~20–8 Ma (**b**); and, after ~8 Ma, Ryukyu slab pull (1) transmitted across the PSP (2) to drive Izu-Bonin advance (3), while Mariana Trough spreading weakens direct coupling (orange) so that the Mariana segment (5) advances mainly through lateral coupling with the faster-advancing Izu-Bonin segment (4) (**c**). **d–f,** West–east cross-sections: normal subduction (**d**); rollback and steepening (**e**); and, after ~8 Ma, trench advance migrating the shallow hinge westward by $\Delta x \approx 100–300$ km while its deep limb migrates westward only slowly (**f**). The resulting kinematic mismatch buckles the

slab into the backward-folded geometry imaged in Fig. 2, accompanied by uplift of hydrous MTZ material (see Fig. 4). Grey dashed curves denote the 20 Ma and 8 Ma plate/slab positions relative to a fixed trench reference (vertical dashed line). Not to scale.

Melt generation behind the slab driven by uplift of MTZ material

The backward folding of the Pacific slab within the MTZ has profound implications for the redistribution of volatile-rich materials and the generation of melts in the overlying upper mantle. The ongoing westward subduction of the Pacific plate, coupled with the rapid westward advance of the IBM trench—the most significant trench advance on Earth today—continuously feeds slab material into the MTZ, whereas the deeper portion of the slab, which has already penetrated the 660-km discontinuity, migrates westward at a significantly slower rate owing to the high viscous resistance of the lower mantle. Because the slab behaves as a quasi-rigid plate of essentially fixed downdip length, this convergence between its fast-advancing shallow hinge and its slowly migrating deep limb reduces the horizontal span available to the slab within the MTZ; the excess slab length is therefore accommodated out of plane and, because the flattened and stacked slab resides longer within the MTZ depth window, the slab volume housed in the transition zone grows with time, displacing an equivalent volume of ambient MTZ material. With downward escape into the high-viscosity lower mantle impeded, the displaced material is preferentially extruded upward above the fold hinge and along the upper surface of the slab, driving a focused upwelling immediately behind (east of) the folded slab. This mechanical extrusion is consistent with geodynamic

models in which slab flattening and folding in the MTZ act as an efficient pump expelling ambient transition-zone material upward[8,43], with the "big mantle wedge" model for East Asia, where plume-like upwellings of MTZ material rise above the flattened Pacific slab[44,45], and with the volume balance of slab migration, which requires that lateral migration and flattening of the slab displace an equivalent volume of surrounding mantle[21,46].

The composition of the upwelled material makes this process consequential. The MTZ is a major reservoir not only for H_2O—stored in wadsleyite and ringwoodite[47,48]—but also for recycled carbon, likely hosted in carbonated eclogite fragments that represent a key component of deep mantle heterogeneity. Consequently, the ambient MTZ material extruded by the folding slab is rich in both H_2O and CO_2. As this material crosses the 410-km discontinuity, the transformation to olivine collapses the water-storage capacity of the residue. Crucially, at these pressures (>~10 GPa), the miscibility gap between aqueous fluids and hydrous silicate melts vanishes[49,50], so the expelled volatile is not a low-density free fluid but a dense supercritical hydrous melt. Furthermore, the combined presence of CO_2 and H_2O drastically depresses the peridotite solidus, inciting deep silicate melting well below the volatile-free solidus[51]. Because this supercritical melt may lack positive buoyancy—the condition central to the "water filter" hypothesis[52]—we propose that in our study region, it is the mechanical pumping by the still-growing backward fold that overcomes this density barrier, forcing the volatile-charged melt upward.

The ascent regime changes in the uppermost mantle. Below ~10 GPa (<~300 km), the miscibility gap reopens and the melt fraction increases as the wet solidus is crossed, allowing buoyancy to take over from mechanical pumping and sustain the ascent. This transition explains why the low-velocity channel

behind the slab becomes most prominent and vertically coherent at 150–300 km and sharpens toward the LAB (Fig. 2). Notably, recent high-pressure experiments demonstrate that volatile-charged (H_2O- and CO_2-bearing) carbonate-rich melts can completely wet olivine grain boundaries, forming highly interconnected permeable networks even at ultralow melt fractions[53]. Such complete wetting provides a robust physical mechanism for the observed −3% to −5% seismic velocity reductions, indicating that a trace amount of highly mobile, carbonated melt is sufficient to generate the prominent low-velocity channel imaged in our model.

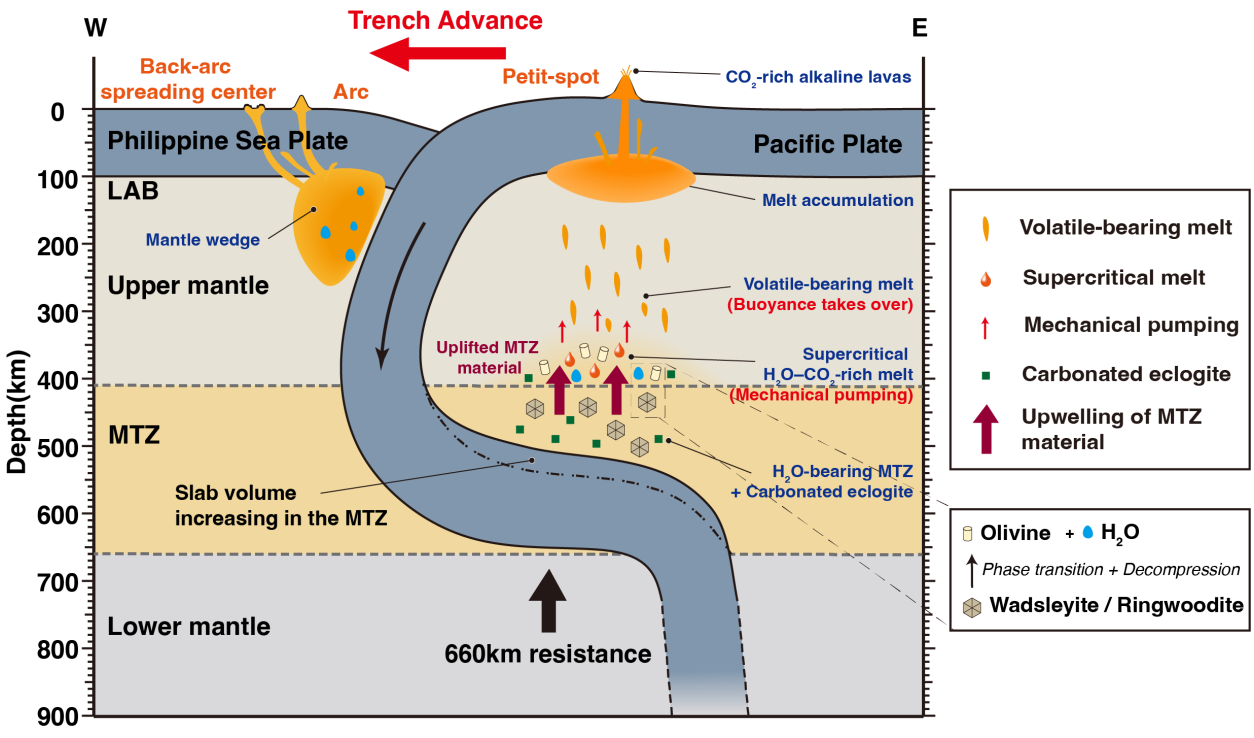


Fig. 4 | Conceptual model for deep melt generation and ascent driven by backward slab folding and volatile (H_2O + CO_2) release. Ongoing subduction combined with trench advance feeds slab material into the MTZ faster than the slowly migrating deep limb escapes, so that the net slab volume within the MTZ grows—

by flattening, stacking and backward folding—and displaces an equivalent volume of ambient MTZ material. This hydrous–carbonated material (wadsleyite/ringwoodite + carbonated eclogite) is extruded upward in the solid state above the fold hinge (magenta arrows). At the 410-km crossing, the combined presence of H_2O and CO_2 drastically depresses the solidus, generating a dense supercritical hydrous-carbonate melt ("water follows carbon"). Because this melt may lack positive buoyancy, its initial ascent is driven by the mechanical pumping of the folding slab. Upon reaching shallower upper-mantle depths (<300 km), the melt fraction increases, buoyancy takes over, and the melt ascends rapidly. Crucially, such melts completely wet olivine grain boundaries, forming interconnected networks at ultralow fractions[53]—sufficient to explain the −3% to −5% dVp channel behind the slab. The melt ultimately accumulates beneath the LAB and leaks through flexure-induced fractures to feed the highly alkaline, CO_2-rich petit-spot volcanism on the incoming plate. Dashed lines denote the LAB and mantle discontinuities; the red arrow indicates trench advance. Not to scale.

Upon reaching the LAB, this volatile- and carbonate-rich melt accumulates as a layered melt body, ponding where viscosity contrasts and density stratification inhibit further ascent[54]. Melt may then leak upward through fractures generated by plate flexure to feed petit-spot volcanism on the incoming plate. This deep-sourced, CO_2-H_2O-driven melting framework elegantly explains the scattered, small-volume nature of the young volcanic edifices and, more importantly, their distinctive geochemical fingerprints. Petit-spot lavas are highly alkaline, silica-undersaturated, and exceptionally enriched in CO_2 and volatiles, with isotopic signatures indicating metasomatized, recycled mantle sources[1,3]. Such compositions explicitly

require the involvement of carbonated melts generated at upper-mantle to transition-zone depths[55], perfectly matching the uplift of carbonated, hydrated MTZ material driven by slab folding.

We note that our interpretation relies on the spatial correlation between the imaged low-velocity channel and the surface distribution of petit-spot volcanoes, combined with geodynamic reasoning. We do not directly observe melt migration from the MTZ to the seafloor, and the seismic resolution at MTZ depths limits our ability to constrain the precise geometry of the uplifted material. Future work combining higher-resolution seismic imaging, petrological modelling, and geochemical analysis of petit-spot lavas will be needed to fully test this hypothesis.

In summary, the backfolded slab geometry imaged beneath the central Mariana provides direct seismological evidence that trench advance can mechanically deform the slab within the MTZ, inducing uplift of hydrous and carbonated phases and triggering localized melting in the overlying upper mantle. The resulting melt represents a plausible deep source for the petit-spot volcanism observed on the incoming Pacific plate. More broadly, given that intense slab deformation in the MTZ is observed along the entire IBM system[35] and that petit-spot volcanism also occurs seaward of the Izu-Bonin segment[2], this mechanism may operate systematically in other subduction zones experiencing trench advance, offering a new perspective on the deep origins of intraplate volcanism.

References

1. Hirano, N. *et al.* Volcanism in Response to Plate Flexure. **313**, (2006).
2. Hirano, N. *et al.* Petit-spot volcanoes on the oldest portion of the Pacific plate. *Deep Sea Res. Part Oceanogr. Res. Pap.* **154**, 103142 (2019).
3. Machida, S. *et al.* Petit-spot geology reveals melts in upper-most asthenosphere dragged by lithosphere. *Earth Planet. Sci. Lett.* **426**, 267–279 (2015).
4. Taneja, R. *et al.* 40 Ar/ 39 Ar geochronology and the paleoposition of Christmas Island (Australia), Northeast Indian Ocean. *Gondwana Res.* **28**, 391–406 (2015).
5. Mikuni, K. *et al.* Lithological structure of western Pacific lithosphere reconstructed from mantle xenoliths in a petit-spot volcano. *Prog. Earth Planet. Sci.* **9**, 62 (2022).
6. Harmon, N. *et al.* Evidence for Petit-Spot Volcanism in the Puerto Rico Trench. *Geophys. Res. Lett.* **52**, e2024GL114362 (2025).
7. Hirano, N. & Machida, S. The mantle structure below petit-spot volcanoes. *Commun. Earth Environ.* **3**, 110 (2022).
8. Yang, J. & Faccenda, M. Intraplate volcanism originating from upwelling hydrous mantle transition zone. *Nature* **579**, 88–91 (2020).
9. Yang, J. *et al.* The origin and fate of subslab partial melts at convergent margins. *Natl. Sci. Rev.* nwaf314 (2025) doi:10.1093/nsr/nwaf314.

10. Koppers, A. A. P., Staudigel, H., Pringle, M. S. & Wijbrans, J. R. Short-lived and discontinuous intraplate volcanism in the South Pacific: Hot spots or extensional volcanism? *Geochem. Geophys. Geosystems* **4**, 2003GC000533 (2003).
11. Wei, X., Zhang, Y., Shi, X. & Zhang, H. Geochronological and geochemical constraints on the petrogenesis and geodynamic process of Hemler, Vlinder, and Il'ichev seamount lavas in NW Pacific. *Sci. China Earth Sci.* **67**, 1856–1871 (2024).
12. Mel'nikov, M. E., Pletnev, S. P., Anokhin, V. M., Sedysheva, T. E. & Ivanov, V. V. Volcanic edifices on guyots of the Magellan Seamounts (Pacific Ocean). *Russ. J. Pac. Geol.* **10**, 435–442 (2016).
13. Peretyazhko, I. S., Savina, E. A. & Pulyaeva, I. A. Miocene Petit-Spot Basanitic Volcanoes on Cretaceous Alba Guyot (Magellan Seamount Trail, Pacific Ocean). *Geosciences* **14**, 252 (2024).
14. Sui, B. *et al.* Late-stage structural evolution from near-bottom topographic and magnetic Surveys of Suda Seamount (West Pacific). *Deep Sea Res. Part Oceanogr. Res. Pap.* **198**, 104053 (2023).
15. Yan, Q., Milan, L., Saunders, J. E. & Shi, X. Petrogenesis of Basaltic Lavas From the West Pacific Seamount Province: Geochemical and Sr-Nd-Pb-Hf Isotopic Constraints. *J. Geophys. Res. Solid Earth* **126**, e2020JB021598 (2021).
16. Ohira, A. *et al.* Seismic Structure of the Oceanic Crust Around Petit-Spot Volcanoes in the Outer-Rise Region of the Japan Trench. *Geophys. Res. Lett.* **45**, (2018).
17. Eimer, M. Seismicity and Shallow Structure at the Mariana Subduction Zone. PhD thesis, Washington Univ. in St. Louis (2020).

18. Tibi, R., Wiens, D. A. & Yuan, X. Seismic evidence for widespread serpentinized forearc mantle along the Mariana convergence margin. *Geophys. Res. Lett.* **35**, 2008GL034163 (2008).

19. Barklage, M. *et al. P* and *S* velocity tomography of the Mariana subduction system from a combined land-sea seismic deployment. *Geochem. Geophys. Geosystems* **16**, 681–704 (2015).

20. Qiao, Q. *et al.* Upper Mantle Structure Beneath Mariana: Insights From Rayleigh-Wave Anisotropic Tomography. *Geochem. Geophys. Geosystems* **22**, e2021GC009902 (2021).

21. Schellart, W. P., Stegman, D. R. & Freeman, J. Global trench migration velocities and slab migration induced upper mantle volume fluxes: Constraints to find an Earth reference frame based on minimizing viscous dissipation. *Earth-Sci. Rev.* **88**, 118–144 (2008).

22. Miller, M. S., Kennett, B. L. N. & Toy, V. G. Spatial and temporal evolution of the subducting Pacific plate structure along the western Pacific margin. *J. Geophys. Res. Solid Earth* **111**, 2005JB003705 (2006).

23. Faccenna, C., Holt, A. F., Becker, T. W., Lallemand, S. & Royden, L. H. Dynamics of the Ryukyu/Izu-Bonin-Marianas double subduction system. *Tectonophysics* **746**, 229–238 (2018).

24. Jian, H. *et al.* Slab Pull Drives IBM Trench Advance Despite the Weakened Philippine Sea Plate. *Geophys. Res. Lett.* **50**, e2023GL106554 (2023).

25. Kang, H. *et al.* Seismic Velocity Structure of Upper Mantle Beneath the Oldest Pacific Seafloor: Insights From Finite-Frequency Tomography. *Geochem. Geophys. Geosystems* **24**, e2022GC010833 (2023).

26. Park, J. Y. *et al.* Detection and Location of the Oceanic Intraplate Earthquakes at the Oldest Pacific Plate Using Pacific Array (Oldest-1) Data. *Seismol. Res. Lett.* **96**, 664–677 (2025).

27. Pozgay, S. H., Wiens, D. A., Conder, J. A., Shiobara, H. & Sugioka, H. Seismic attenuation tomography of the Mariana subduction system: Implications for thermal structure, volatile distribution, and slow spreading dynamics. (2009).

28. Cai, C., Wiens, D. A., Shen, W. & Eimer, M. Water input into the Mariana subduction zone estimated from ocean-bottom seismic data. *Nature* **563**, 389–392 (2018).

29. Dahlen, F. A. Fre® chet kernels for ¢nite-frequency traveltimesˆI. Theory. (2000).

30. Yang, T. *et al.* Seismic structure beneath the Rivera subduction zone from finite-frequency seismic tomography. *J. Geophys. Res. Solid Earth* **114**, 2008JB005830 (2009).

31. Hung, S., Shen, Y. & Chiao, L. Imaging seismic velocity structure beneath the Iceland hot spot: A finite frequency approach. *J. Geophys. Res. Solid Earth* **109**, 2003JB002889 (2004).

32. Fukao, Y., Obayashi, M., Nakakuki, T., & the Deep Slab Project Group. Stagnant Slab: A Review. *Annu. Rev. Earth Planet. Sci.* **37**, 19–46 (2009).

33. Fukao, Y. & Obayashi, M. Subducted slabs stagnant above, penetrating through, and trapped below the 660 km discontinuity. *J. Geophys. Res. Solid Earth* **118**, 5920–5938 (2013).

34. Jaxybulatov, K., Koulakov, I. & Dobretsov, N. L. Segmentation of the Izu-Bonin and Mariana slabs based on the analysis of the Benioff seismicity distribution and regional tomography results. *Solid Earth* **4**, 59–73 (2013).

35. Zhang, H. & Wang, F. Slab morphology and deformation beneath Izu-Bonin. (2019).

338 36. Čížková, H. & Bina, C. R. Geodynamics of trench advance: Insights from a Philippine-Sea-style
339 geometry. *Earth Planet. Sci. Lett.* **430**, 408–415 (2015).
340 37. Garel, F. *et al.* Interaction of subducted slabs with the mantle transition-zone: A regime diagram from
341 2-D thermo-mechanical models with a mobile trench and an overriding plate. *Geochem. Geophys.*
342 *Geosystems* **15**, 1739–1765 (2014).
343 38. Carlson, R. L. & Mortera-Gutiérrez, C. A. Subduction hinge migration along The Izu-Bonin-Mariana
344 arc. *Tectonophysics* **181**, 331–344 (1990).
345 39. Gianni, G. M., Guo, Z., Holt, A. F. & Faccenna, C. Non-collisional orogeny in northeast Japan driven
346 by nearby same-dip double subduction. *Nat. Geosci.* **18**, 525–533 (2025).
347 40. Ribe, N. M. Bending mechanics and mode selection in free subduction: a thin-sheet analysis. *Geophys.*
348 *J. Int.* **180**, 559–576 (2010).
349 41. Stegman, D. R., Schellart, W. P. & Freeman, J. Competing influences of plate width and far-field
350 boundary conditions on trench migration and morphology of subducted slabs in the upper mantle.
351 *Tectonophysics* **483**, 46–57 (2010).
352 42. Karato, S., Riedel, M. R. & Yuen, D. A. Rheological structure and deformation of subducted slabs in
353 the mantle transition zone: implications for mantle circulation and deep earthquakes. *Phys. Earth*
354 *Planet. Inter.* **127**, 83–108 (2001).
355 43. Zhou, L. *et al.* Slab flattening in the mantle transition zone drives extrusion and upwelling of ancient
356 subducted material. *Earth Planet. Sci. Lett.* **690**, 120185 (2026).

44. Zhao, D., Maruyama, S. & Omori, S. Mantle dynamics of Western Pacific and East Asia: Insight from seismic tomography and mineral physics. *Gondwana Res.* **11**, 120–131 (2007).

45. Maruyama, S., Santosh, M. & Zhao, D. Superplume, supercontinent, and post-perovskite: Mantle dynamics and anti-plate tectonics on the Core–Mantle Boundary. *Gondwana Res.* **11**, 7–37 (2007).

46. Garfunkel, Z., Anderson, C. A. & Schubert, G. Mantle circulation and the lateral migration of subducted slabs. *J. Geophys. Res. Solid Earth* **91**, 7205–7223 (1986).

47. Kohlstedt, D. L., Keppler, H. & Rubie, D. C. Solubility of water in the α, β and γ phases of (Mg,Fe)2SiO4. *Contrib. Mineral. Petrol.* **123**, 345–357 (1996).

48. Pearson, D. G. *et al.* Hydrous mantle transition zone indicated by ringwoodite included within diamond. *Nature* **507**, 221–224 (2014).

49. Mibe, K. *et al.* Second critical endpoint in the peridotite-H_2 O system. *J. Geophys. Res. Solid Earth* **112**, 2005JB004125 (2007).

50. Kawamoto, T., Kanzaki, M., Mibe, K., Matsukage, K. N. & Ono, S. Separation of supercritical slab-fluids to form aqueous fluid and melt components in subduction zone magmatism. *Proc. Natl. Acad. Sci.* **109**, 18695–18700 (2012).

51. Dasgupta, R., Hirschmann, M. M. & Smith, N. D. Water follows carbon: CO2 incites deep silicate melting and dehydration beneath mid-ocean ridges. *Geology* **35**, 135 (2007).

52. Bercovici, D. & Karato, S. Whole-mantle convection and the transition-zone water filter. *Nature* **425**, 39–44 (2003).

53. Huang, Y. *et al.* Upper mantle low-velocity layer tied to volatile-charged carbonate melts. *Sci. Adv.* (2026).

54. Zhang, J. *et al.* Seismic Imaging of Upper Mantle Serpentinization and Ponded Melt at the Boundary of the Lithosphere and Asthenosphere in the Central Mariana Subduction Zone. *Geophys. Res. Lett.* **52**, e2025GL119716 (2025).

55. Dasgupta, R. *et al.* Carbon-dioxide-rich silicate melt in the Earth's upper mantle. *Nature* **493**, 211–215 (2013).

Methods

Seismic data collection and processing

This study integrates seismic data from multiple deployments in the Mariana region (Fig. 1): (1) 9 ocean-bottom seismometers (OBSs) deployed in 2021–2022 as part of an experiment studying petit-spot volcano origins by the Southern University of Science and Technology (SUSTech); (2) 11 OBSs from the Oldest-1 experiment (October 2018–November 2019)[25]; and (3) previously recorded data from US-led experiments near the Mariana Trench in 2003–2004[27] and in 2011-2012[28]. Our dataset comprises 51 OBS stations and 53 island-based stations, with most OBS deployments operating continuously for over one year. Seafloor seismic data underwent corrections for tilt and compliance noise prior to analysis[56]. We selected teleseismic events with magnitudes $Mw \geq 5.5$ and epicentral distances of 28°–105° for P-wave phases (Fig. 1).

Finite-frequency tomography and inversion strategy

We employed finite-frequency seismic tomography (FFST), which accounts for the finite-frequency nature of seismic waves and their sensitivity to three-dimensional structures surrounding the ray path[29]. To maximize resolution across multiple spatial scales, we implemented a multi-frequency inversion strategy[30,31,57] that significantly improves utilization of broadband data, particularly for seafloor recordings. Vertical-component waveforms were filtered into three frequency bands: high (0.5–2 Hz), intermediate (0.1–0.5 Hz), and low (0.03–0.1 Hz). Waveform data were initially screened by applying signal-to-noise

ratio (SNR) thresholds specific to each frequency band, and all waveforms passing these thresholds were subsequently verified by visual inspection. From 487 events recorded by 104 stations, we obtained 5,850 relative P-wave arrival times (Extended Data Figs. 1 and 2). To address the significant seafloor topography variations, we applied frequency-dependent crustal corrections[58] based on the CRUST1.0 model[59]. Station terms were incorporated into the inversion to further reduce crustal influences.

To minimize boundary effects, we adopted a broad model domain centered at (16°N, 151°E), spanning 27° in longitude, 16° in latitude, and extending to 900 km depth, so that the slab can be traced across the 660-km discontinuity without bottom-edge artifacts. This domain was discretized into a 55 × 33 × 31 grid with 0.5° horizontal and 30 km vertical spacing for three-dimensional P-wave velocity inversion (Extended Data Fig. 3a). Optimal values for the smoothing and damping parameters were determined through trade-off analysis (Extended Data Fig. 3b). The inversion was solved using the LSQR algorithm.

Resolution assessment

We conducted comprehensive checkerboard resolution tests and feature-specific recovery tests to evaluate the spatial reliability of our tomographic model. We acknowledge that the ocean-bottom recordings are of lower quality than the land data and that the station distribution is uneven; consequently, resolution is heterogeneous across the model. Vertical checkerboard tests indicate that resolution along profiles A–A’ and D–D’ is relatively limited owing to sparse station coverage, whereas profiles B–B’ and C–C’ exhibit moderate smearing toward the western side (Extended Data Fig. 5). Horizontal checkerboard

tests demonstrate reliable recovery in shallow regions beneath the station coverage but strong smearing at depths greater than 390 km (Extended Data Fig. 6). Targeted recovery tests show that the first-order anomaly patterns—including the western low-velocity anomaly, the central high-velocity slab, and the eastern low-velocity channel—are robustly recovered (Extended Data Fig. 7).

A particular concern for this study is whether the backward-folded slab geometry imaged in the MTZ could be an artifact of ray-path smearing, given the uneven earthquake distribution. Two considerations argue against this. First, smearing is controlled by the local ray geometry: because earthquakes to the east of the study area are scarce, no ray paths exist that could stretch the steeply dipping slab anomaly eastward into a spurious sub-horizontal fold, and any residual smearing would produce sub-vertical streaks rather than the coherent eastward-bending anomaly we image. Second, a dedicated restoration test using an input model containing a backward-folded high-velocity slab flanked by −3% low-velocity anomalies (Extended Data Fig. 8) recovers the folded geometry closely, particularly along profiles C–C’ and D–D’, without introducing artificial eastward smearing. Together, these tests confirm that the backward folding represents a genuine feature of the subducting slab rather than an inversion artifact.

To further verify the robustness of the key features against the uneven ray coverage and noise inherent to the ocean-bottom data, we randomly divided the full dataset into two halves and performed two independent inversions (Extended Data Figs. 9 and 10). As expected for halved datasets, the resolution is somewhat reduced and the anomaly amplitudes are slightly weaker than in the full-dataset model. Nevertheless, both half-dataset models reproduce the first-order structures, including the steeply dipping slab, the backward fold within the MTZ, and the low-velocity channel behind the slab. The consistency

between the two independent inversions demonstrates that these features are not controlled by any particular subset of events or stations, nor by localized noise sources, and provides additional confidence in the interpretations presented in the main text.

With the grid deepened to 900 km, the vertical checkerboard test (Extended Data Fig. 5) shows that resolution below ~700 km is limited; accordingly, the lower-mantle anomaly is interpreted only in terms of its lateral position relative to the folded slab. A recovery test using an input slab that extends into the lower mantle (Extended Data Fig. 8) reproduces both the backward fold and the deep high-velocity continuation, supporting their robustness.

Data Availability

Seismic data of US-led experiments and the Oldest-1 experiment are available from the Data Management Centers of U.S. Earthscope and the Ocean Hemisphere Project (OHP), respectively, while the SUSTech data can be accessed at the Data Center of the OBS Laboratory at SUSTech (https://obslab.sustech.edu.cn/data/). Generic Mapping Tools (GMT) were used to generate the figures[60] (https://www.generic-mapping-tools.org/), and SAC was employed for data processing[61].

References

56. Bell, S. W., Forsyth, D. W. & Ruan, Y. Removing Noise from the Vertical Component Records of Ocean-Bottom Seismometers: Results from Year One of the Cascadia Initiative. *Bull. Seismol. Soc. Am.* **105**, 300–313 (2015).

57. Yang, T., Shen, Y., Vanderlee, S., Solomon, S. & Hung, S. Upper mantle structure beneath the Azores hotspot from finite-frequency seismic tomography. *Earth Planet. Sci. Lett.* **250**, 11–26 (2006).

58. Yang, T. & Shen, Y. Frequency-Dependent Crustal Correction for Finite-Frequency Seismic Tomography. *Bull. Seismol. Soc. Am.* **96**, 2441–2448 (2006).

59. Laske, G., Masters, G., Ma, Z. & Pasyanos, M. Update on CRUST1.0 - A 1-degree Global Model of Earth's Crust.

60. Wessel, P. *et al.* The Generic Mapping Tools Version 6. *Geochem. Geophys. Geosystems* **20**, 5556–5564 (2019).

61. Goldstein, P., Dodge, D., Firpo, M. & Minner, L. 85.5 SAC2000: Signal processing and analysis tools for seismologists and engineers. in *International Geophysics* vol. 81 1613–1614 (Elsevier, 2003).

Acknowledgements

This study is supported by the National Key Research and Development Program of China (2024YFF0808201), the National Natural Science Foundation of China (42327804, 92058209), the High-Level Special Fund of SUSTech (G03050K001).

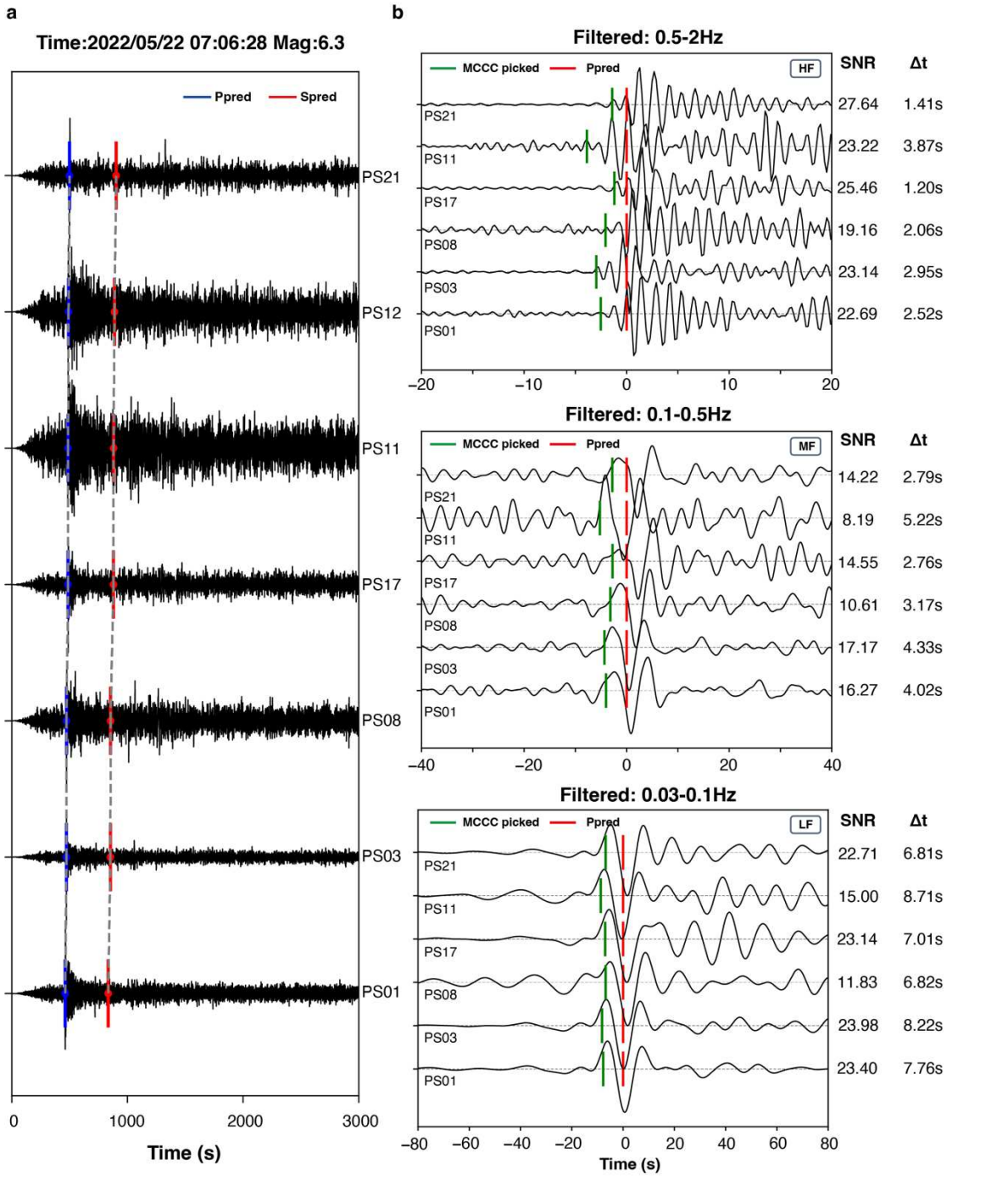
Author contributions

J.L., T.Y. and S.J. designed the methodology and carried out the main data analysis in this research. T.Y. conceived the idea and provides guidance on the genetic mechanisms of petit-spot volcanoes. J.L. and T.Y. wrote the initial draft of the paper. T.Y., Z.L., Y.C. and D.A.W. participated in the discussion and editing of the paper and gave final approval for publication.

Competing interests

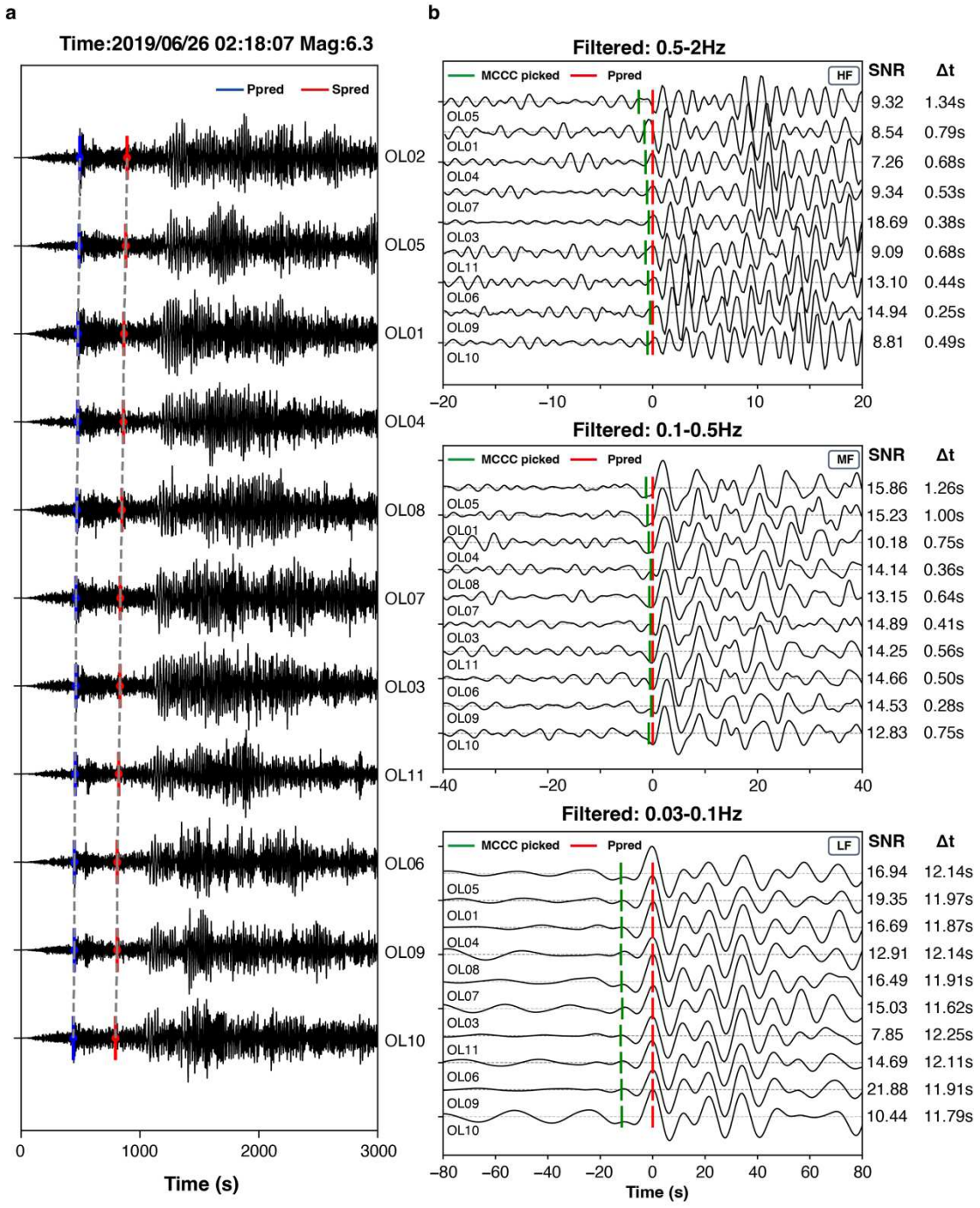
The authors declare no competing interests.

Extended data



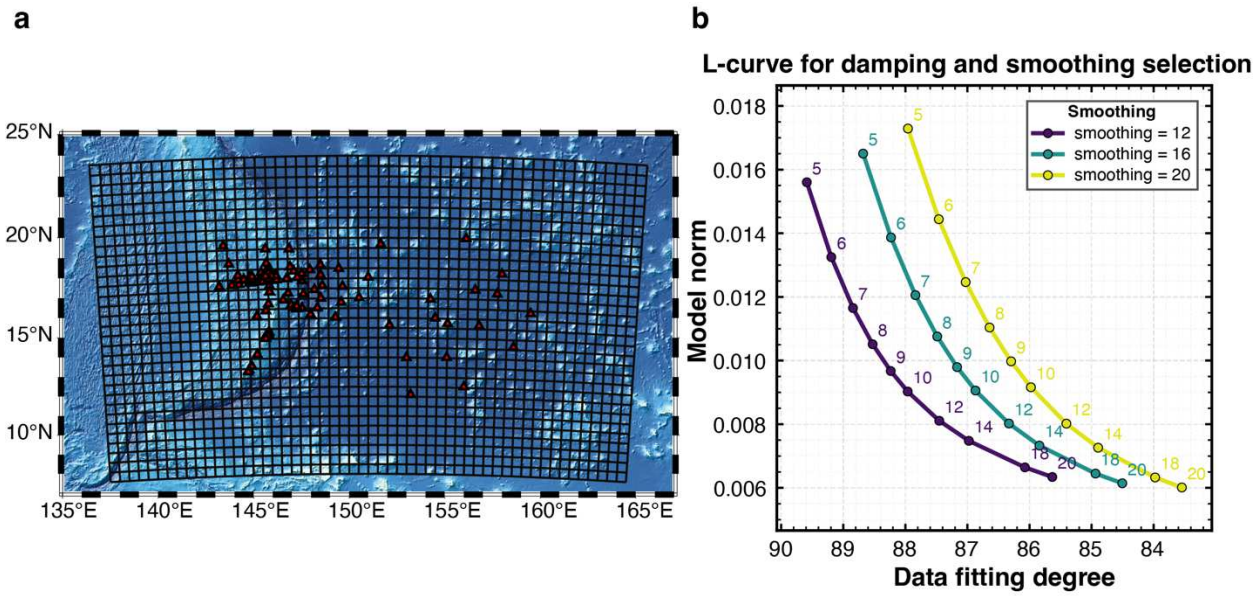
Extended Data Fig. 1 | Example of broadband waveform quality and arrival-time picking used for finite-frequency tomography. (a) Vertical-component seismograms for a Mw 6.3 earthquake recorded by stations of the temporary OBS network, which was deployed during 2021–2022 by the OBS Lab at the

Southern University of Science and Technology and consisted of 9 Pankun OBSs. The waveforms were band-pass filtered between 0.03 and 2 Hz. Predicted P- and S-wave arrivals are marked by blue and red lines, respectively. Predicted P- and S-wave arrivals are marked by blue and red lines, respectively. **(b)** Waveforms filtered in the high-, intermediate-, and low-frequency bands of 0.5–2 Hz, 0.1–0.5 Hz, and 0.03–0.1 Hz, respectively. Green lines denote MCCC-picked P arrivals, whereas red lines denote predicted P arrivals. SNR values and arrival-time residuals relative to the predicted arrivals are listed for each trace.



Extended Data Fig.2 | Example of broadband waveform quality and arrival-time picking used for finite-frequency tomography. (a) Vertical-component seismograms for a representative Mw 6.8 earthquake recorded by stations of the temporary Oldest-1 OBS network, which was deployed during 2018–

2019 and consisted of 11 OBSs. The waveforms were band-pass filtered between 0.03 and 2 Hz. Predicted P- and S-wave arrivals are marked by blue and red lines, respectively. Predicted P- and S-wave arrivals are marked by blue and red lines, respectively. **(b)** Waveforms filtered in the high-, intermediate-, and low-frequency bands of 0.5–2 Hz, 0.1–0.5 Hz, and 0.03–0.1 Hz, respectively. Green lines denote MCCC-picked P arrivals, whereas red lines denote predicted P arrivals. SNR values and arrival-time residuals relative to the predicted arrivals are listed for each trace.



509

510 **Extended Data Fig. 3 | Inversion grid and regularization-parameter selection. (a)** Map view of the

511 model domain and horizontal inversion grid used for finite-frequency P-wave tomography. Black lines

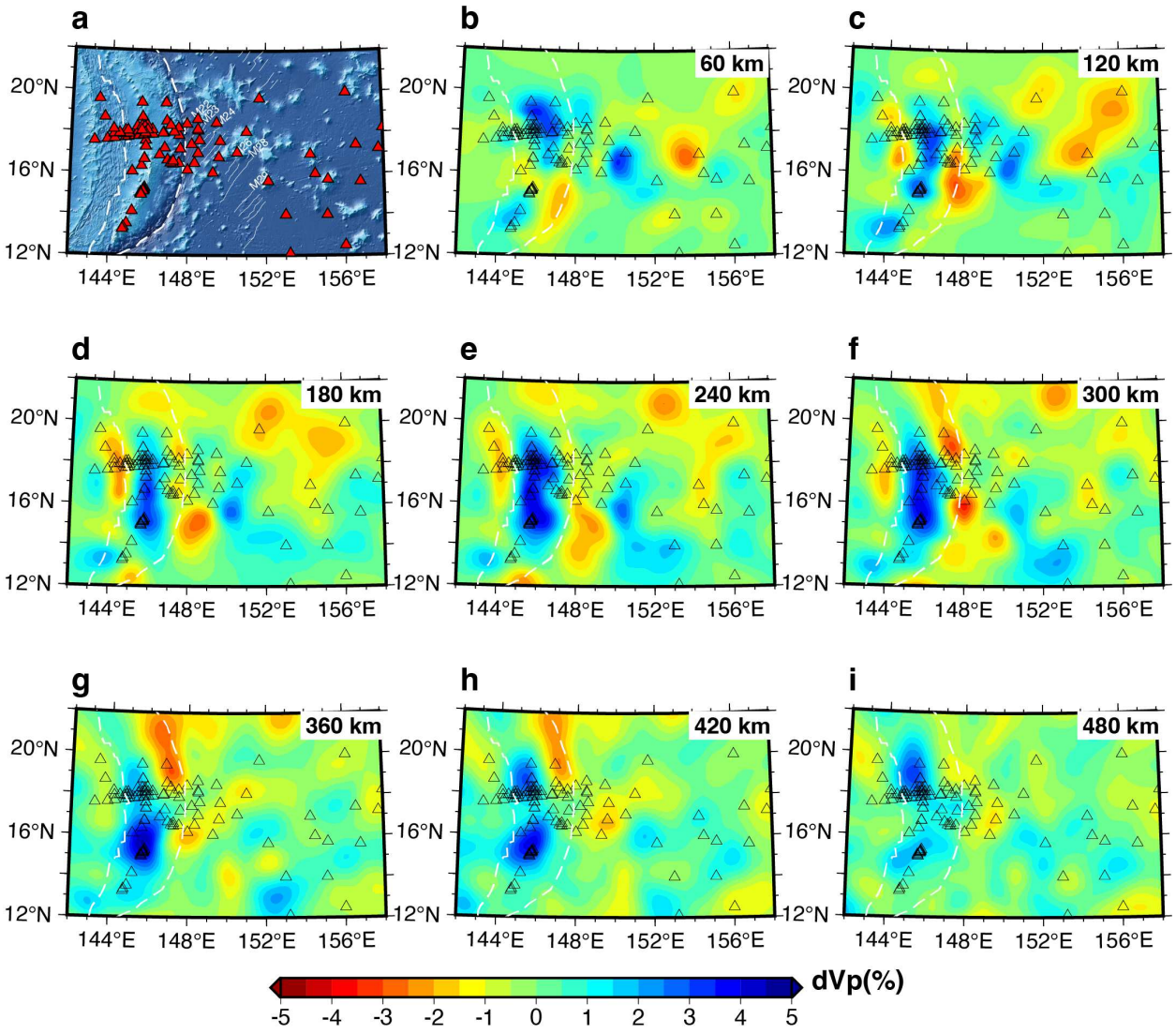
512 show the 0.5° horizontal grid, and red triangles indicate seismic stations. The model extends to 900 km

513 depth with 30 km vertical spacing. **(b)** L-curve trade-off analysis for selecting damping and smoothing

514 parameters. Different curves correspond to different smoothing values, and numbers mark damping

515 parameters.

516



517

518 **Extended Data Fig. 4 | Horizontal depth slices of the finite-frequency P-wave tomographic model. (a)**

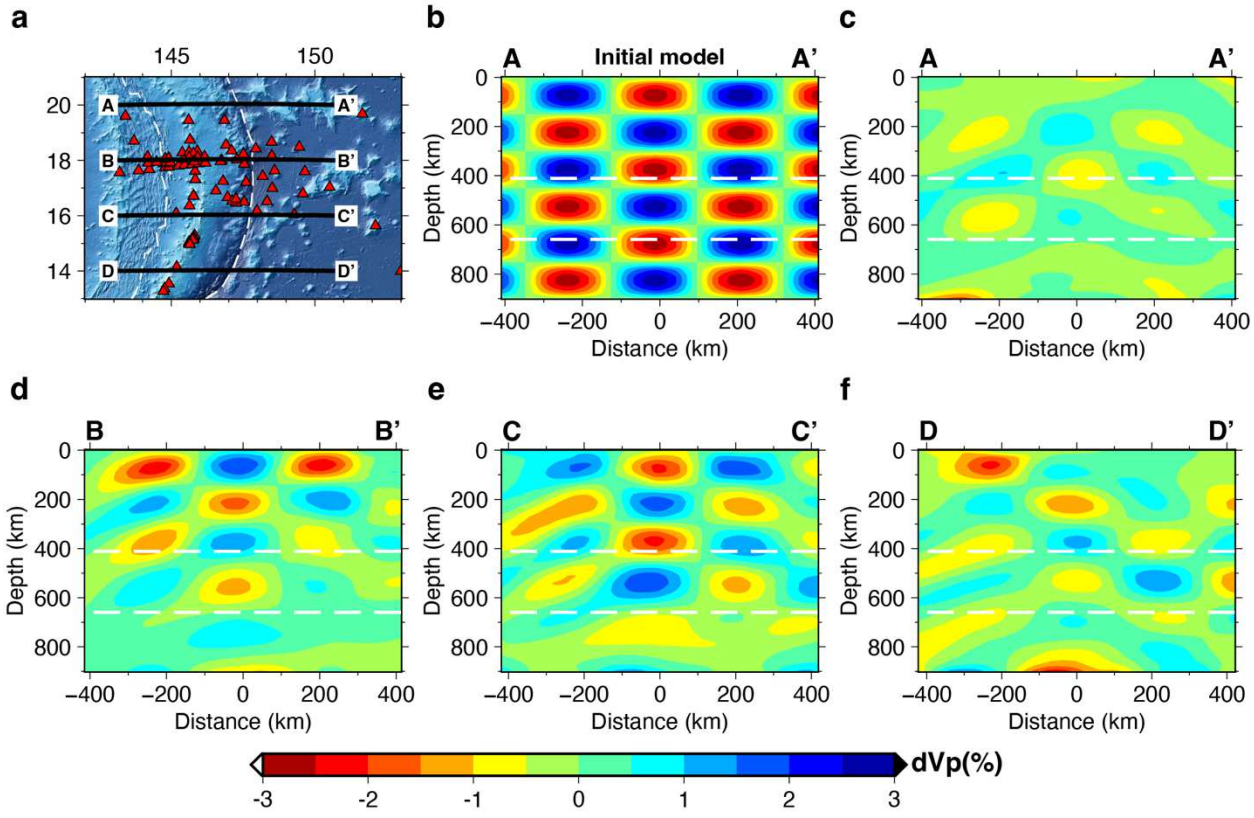
519 Bathymetry and station distribution in the central Mariana region. Red triangles indicate seismic stations

520 used in the inversion. **(b)–(i)** Map views of P-wave velocity perturbations, dVp, at depths of 60, 120, 180,

521 240, 300, 360, 420 and 480 km, respectively. Open triangles mark station locations, and white dashed lines

522 denote the plate boundaries.

523



524

525 **Extended Data Fig. 5 | Vertical checkerboard resolution test with the grid extended to 900 km depth.**

526 **(a)** Bathymetric map showing the station distribution and the locations of the vertical cross sections. Red

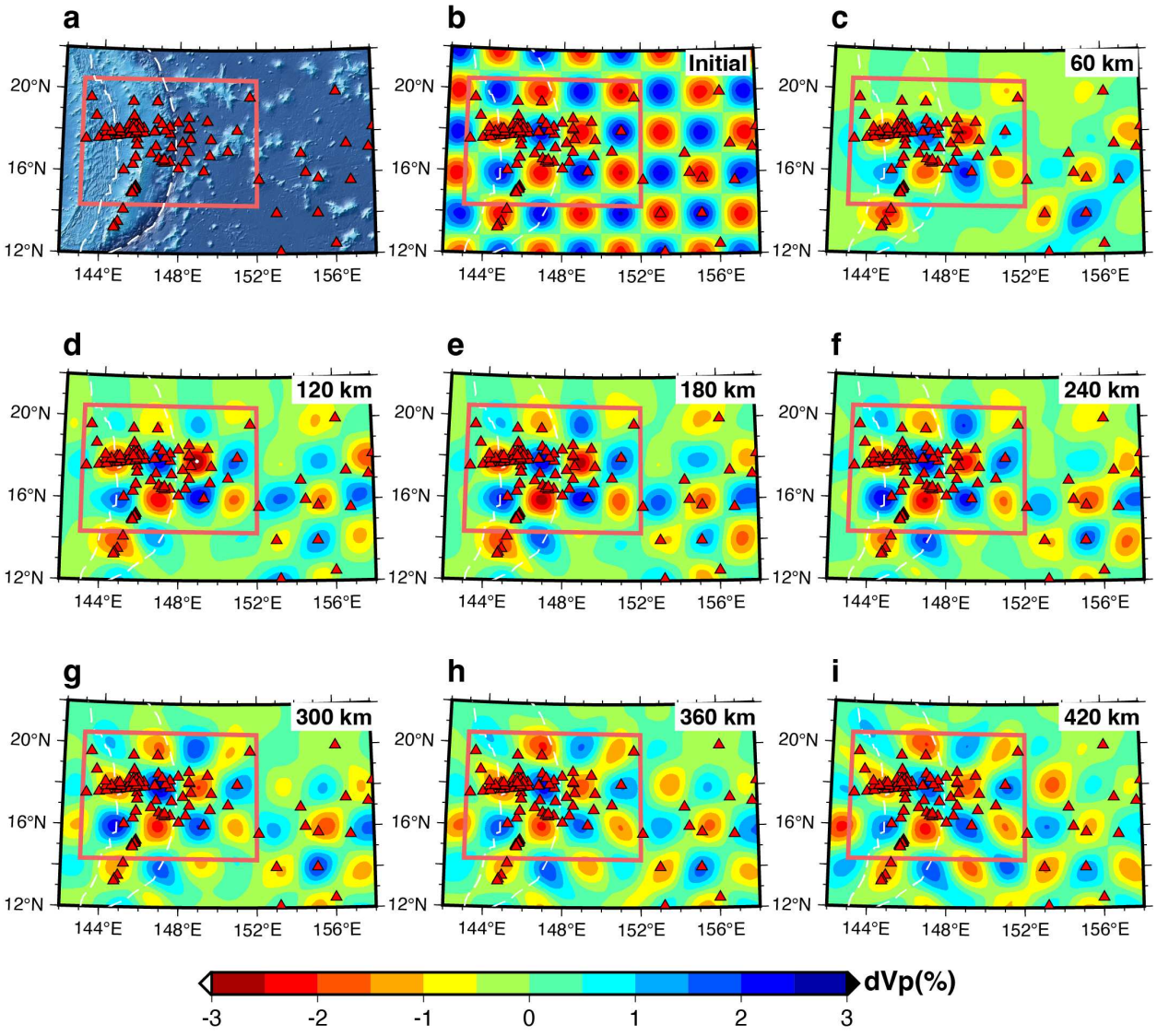
527 triangles indicate seismic stations. **(b)** Input checkerboard model along profile A–A', with alternating ±3%

528 P-wave velocity perturbations and a vertical size of 120 km. **(c)–(f)** Recovered checkerboard models along

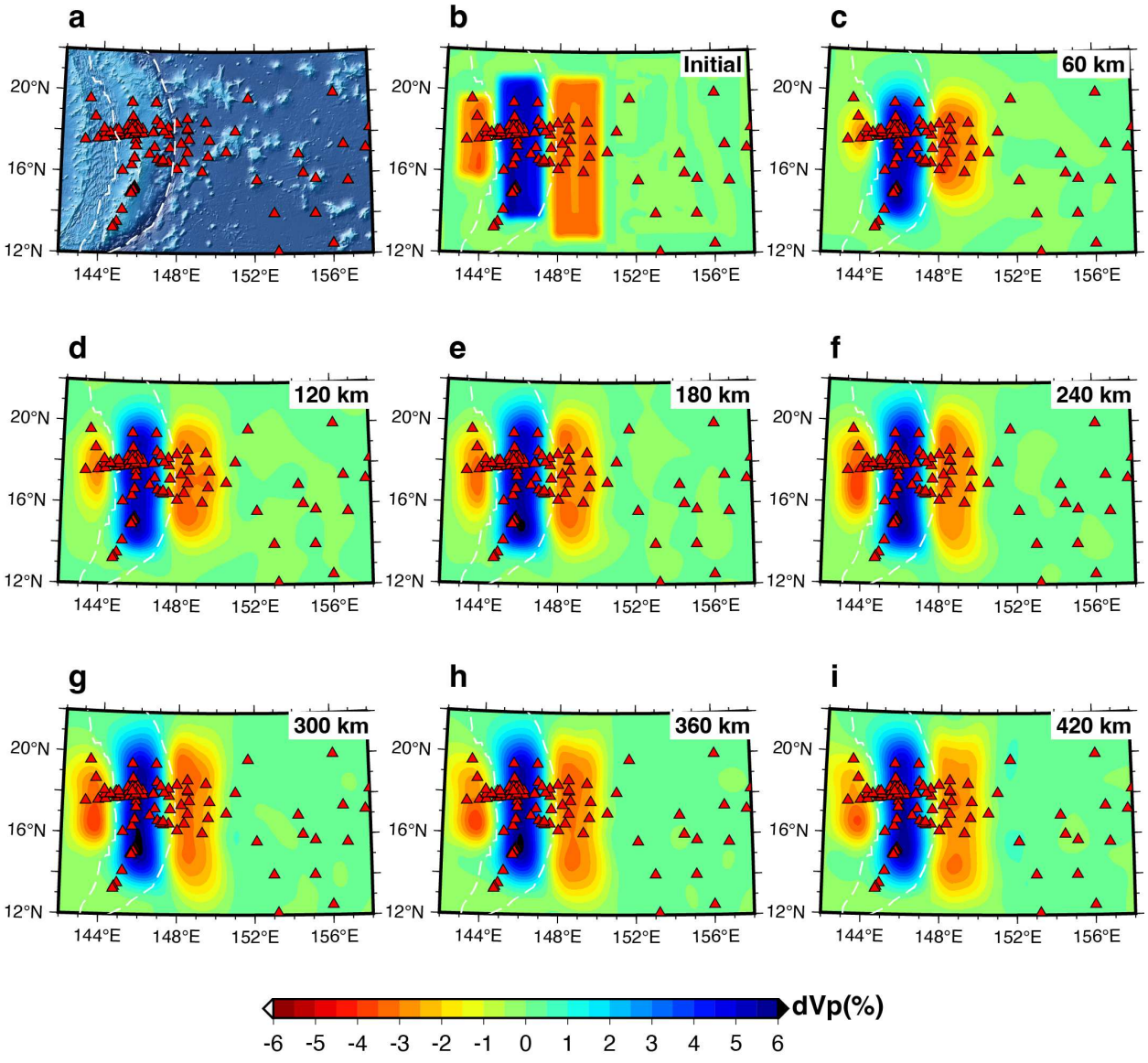
529 profiles A–A', B–B', C–C' and D–D', respectively. White dashed lines mark the 410-km and 660-km

530 discontinuities, and the color scale shows dVp in percent.

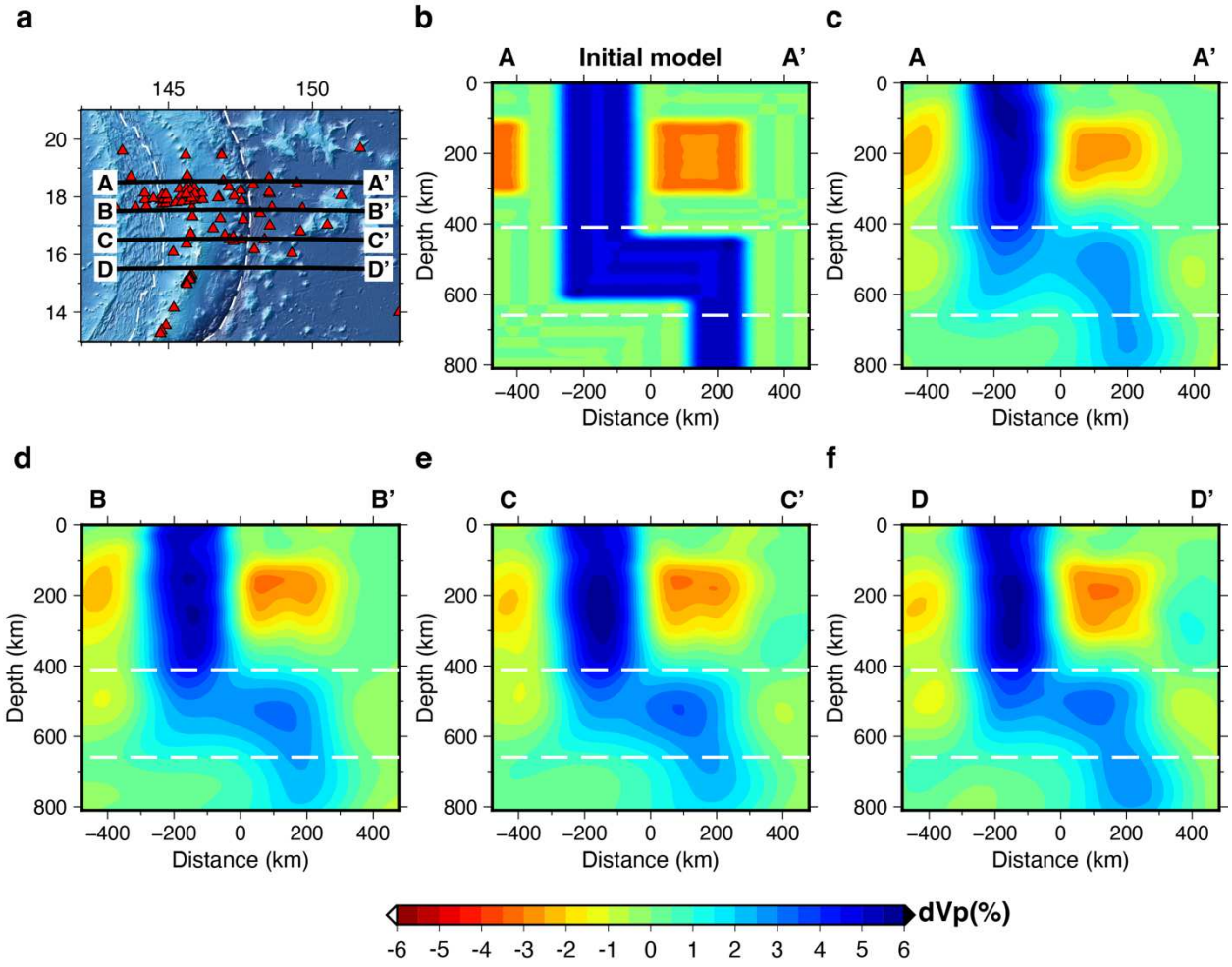
531



Extended Data Fig. 6 | Horizontal checkerboard resolution test. (a) Bathymetry and station distribution in the central Mariana region. The red rectangle outlines the study area focused on in this work. (b) Input checkerboard model with alternating ±3% P-wave velocity perturbations and a horizontal size of 2° × 2°. **(c)–(i)** Recovered models at depths of 60–420 km. The main anomaly is recovered beneath the dense station coverage, demonstrating reliable lateral resolution in the central part of the model. Red triangles indicate seismic stations, white dashed lines denote the plate boundaries, and the color scale shows dVp in percent.



Extended Data Fig. 7 | Feature synthetic recovery test. (a) Bathymetric map showing the distribution of seismic stations used in this study. Red triangles denote station locations, and white dashed lines indicate the plate boundaries. **(b)** Input synthetic model, which includes a western low-velocity anomaly, a central high-velocity anomaly, and an eastern low-velocity anomaly. Velocity perturbations of −3% and +5% were assigned to the low- and high-velocity bodies, respectively. **(c)–(i)** Recovered models at depths of 60–420 km.



547

548 **Extended Data Fig. 8 | Recovery test for the folded-slab geometry using an input model in which the**

549 **high-velocity slab extends into the lower mantle, after deepening the grid to 900 km. (a)** Station

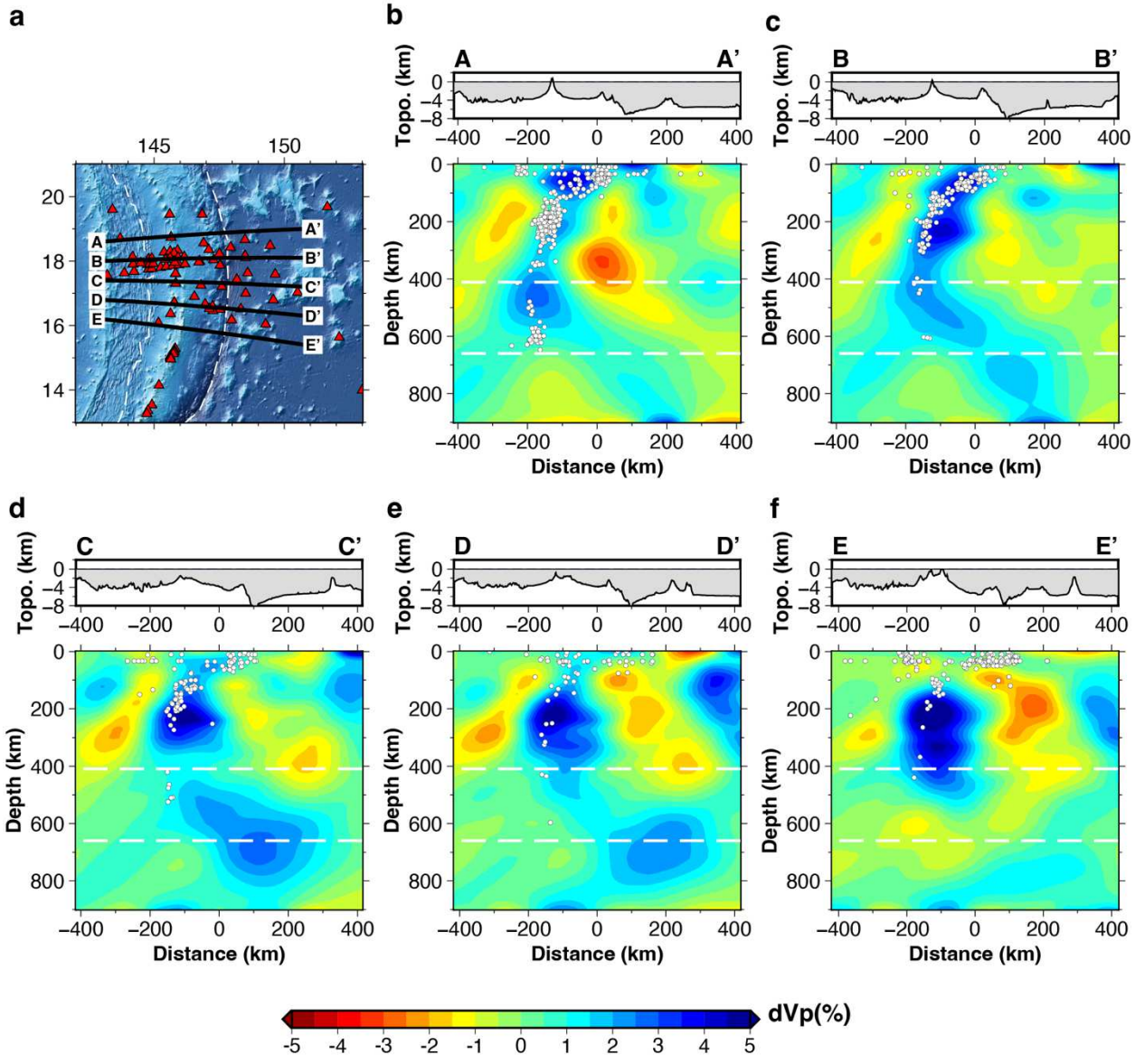
550 distribution and locations of the vertical profiles A–A' to D–D'. Red triangles denote seismic stations. **(b)**

551 Input synthetic model containing a high-velocity anomaly with a backward-folded geometry, flanked by

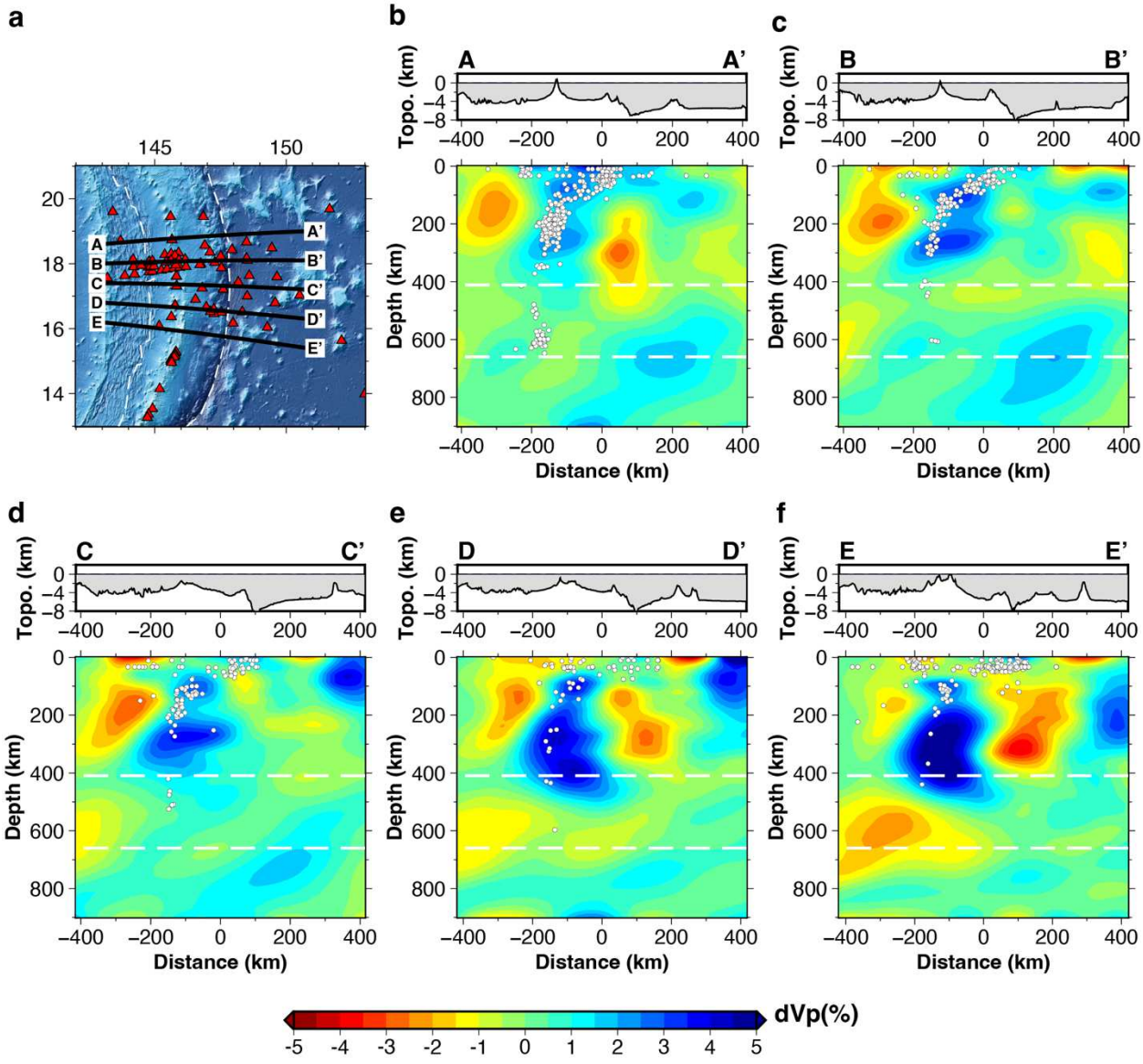
552 low-velocity anomalies. **(c)–(f)** Recovered models along profiles A–A' to D–D'. White dashed lines

553 indicate the 410-km and 660-km discontinuities.

554



Extended Data Fig. 9 | Resolution test using a randomly selected half of the dataset. (a) Map showing the locations of the vertical cross-sections (A–A' to E–E'). **(b)–(f)** Vertical cross-sections of the P-wave velocity perturbation models obtained from inversions using a randomly selected 50% subset of the original dataset, along profiles A–A' to E–E', respectively. Topography is shown above each profile, and the color scale indicates P-wave velocity perturbations relative to the reference model.



Extended Data Fig. 10 | Resolution test using the complementary half of the dataset. Same layout as Extended Data Fig. 9, but using the complementary 50% subset of the original dataset. The first-order features (steeply dipping slab, backward fold in the MTZ, and the low-velocity channel behind the slab) are reproduced in both independent inversions.